Transient numerical modelling of a thermoelectric generator system used for automotive exhaust waste heat recovery

Ding Luo[a,b], Ruochen Wang[a,*], Yuying Yan[b,**], Wei Yu[a], Weiqi Zhou[a]

[a] School of Automobile and Traffic Engineering, Jiangsu University, Zhenjiang, 212013, China

[b] Faculty of Engineering, University of Nottingham, University Park, Nottingham, UK

Corresponding author: * wrc@ujs.edu.cn; ** yuying.yan@nottingham.ac.uk

Abstract: The automotive thermoelectric generator system is a promising technology of exhaust waste heat recovery, but reasonable theoretical models to predict its dynamic performance are lacking. In this work, a transient fluid-thermal-electric multiphysics coupling field numerical model is proposed for the first time, and the model is used to evaluate the dynamic performance of a simplified automotive thermoelectric generator system under vehicle driving cycles. The transient numerical model, which takes into account the dynamic characteristics, fluid-thermal-electric multiphysics field coupling effects, and material temperature dependence, is thus far the most complete model ever. Numerical results reveal that there is a delay in output response with the change of exhaust temperature, and the change of output voltage and output power is often accompanied by the change of exhaust mass flow rate. The small and short-term fluctuation of exhaust gases has a slight influence on output performance. With the transient variation of exhaust characteristics, the output voltage and output power show more stable changes and slower responses, but the situation is the opposite for conversion efficiency. The output power predicted by steady-state numerical simulation is 12.6% higher than that of transient numerical simulation. Moreover, the proposed transient numerical model is recommended to investigate the dynamic performance of automotive thermoelectric generator systems.

Keywords: Thermoelectric generator; Waste heat; Transient numerical model; Multiphysics; Dynamic performance

Nomenclature

Symbols

c	specific heat, $J \cdot kg^{-1} \cdot K^{-1}$
$\vec{E}$	electric field density vector, $V \cdot m^{-2}$
h	convective heat transfer coefficient, $W \cdot m^{-2} \cdot K^{-1}$
$\vec{J}$	current density vector, $A \cdot m^{-2}$
k	turbulent kinetic energy, $m^2 \cdot s^{-2}$
$\dot{m}$	mass flow rate, $g \cdot s^{-1}$
p	pressure, Pa
P	output power, W
Q	heat flux, W
R	resistance, Ω
$\dot{S}$	source term
t	time, s
T	temperature, K
U	output voltage, V
$\vec{v}$	Velocity, $m \cdot s^{-1}$

Greek symbols

ρ	density, $kg \cdot m^{-3}$
μ	dynamic viscosity, Pa·s
λ	thermal conductivity, $W \cdot m^{-1} \cdot K^{-1}$
ε	turbulent dissipation rate, $m^2 \cdot s^{-3}$
σ	electrical conductivity, $S \cdot m^{-1}$
σ^{-1}	electrical resistivity, Ω·m
ϕ	electrical potential, V
α	Seebeck coefficient, $\mu V \cdot K^{-1}$
η	conversion efficiency

Subscripts

co	copper
ex	exhaust gas
ext	external environment
h	hot side
L	load resistance
m	material name
n	n-type thermoelectric material
out	outlet surface
p	p-type thermoelectric material

Abbreviations

CFD	computational fluid dynamics
ECE	economic commission for Europe
TEM	thermoelectric module
TEG	thermoelectric generator

1. Introduction

The development of the automotive industry for the next stage aims to reduce fuel consumption and environmentally harmful emissions [1]. Despite its advantages of no emissions and low noise, electric vehicles suffer from long charging periods, short battery lives, and few charging stations, all of which substantially limit their wide application. At present, engine-powered vehicles are still dominant in the automotive market, and this situation will continue for a long time. Considering that a considerable part of the total energy generated by burning fuel [2] is directly discharged into the environment as waste heat, about 30%, researchers have developed some alternative energy techniques to recover this kind of waste heat, including thermoelectric generator (TEG) systems [3, 4] and organic Rankine cycle (ORC) systems [5]. Used in automotive waste heat recovery, the TEG system is a more feasible approach because of its light weight, small size, and no moving parts [6], among other merits, while the ORC system is more suitable for large-scale transportation equipment driven by engines.

A great number of TEG system prototypes have been fabricated and applied to recycle exhaust waste heat. Zhang et al. [7] manufactured a 1 kW TEG system to recover waste heat from an automotive

diesel engine; the system was comprised of 5 layers of heat exchangers, 6 layers of heat sinks, and 400 thermoelectric modules (TEMs). Through an experimental demonstration, it delivered 1002.6 W electricity under the intake temperature of 500 ℃ and the intake flow rate of 480 g/s. Frobenius et al. [8] integrated a special TEG system with 224 BiTe TEMs into the exhaust after-treatment box of a combustion engine-powered vehicle. The experimental results showed that the output power of 416 W was reached at an exhaust temperature of 300 ℃ and an exhaust mass flow of 1000 kg/h, and the automotive TEG system enabled a potential to become a promising technology for exhaust waste heat recovery. Yang et al. [9] integrated a three-way catalytic converter (TWC) into an automotive TEG system and found that a higher output power and a more uniform temperature distribution could be achieved with a TWC configured in the rear of the heat exchanger. In consideration of the limited space of an automobile exhaust system, Wan et al. [10] proposed and constructed a highly integrated automotive thermoelectric generator (IATEG) system comprised of a cylindrical TEG containing 306 TEMs, a TWC, and a muffler. Through an engine bench test, the developed IATEG system could reach a maximum output power of 515 W at an engine power of 30.4 kW as well as a good acoustic performance.

In addition, many theoretical models have been proposed to assess the behaviour of automotive TEG systems, including computational fluid dynamics (CFD) models [11, 12] and analytical models [13, 14], which can substantially save time and costs when conducting the optimization of TEG systems compared with experimental methods. On the basis of a thermal resistance network and an energy balance, Wang et al. [15] proposed an analytical model to assess the output power and conversion efficiency of a TEG device using exhaust gases as a heat source. The proposed model could be extended to the whole automotive TEG system. Despite the long execution time, CFD models can obtain the detailed temperature and pressure distributions of the automotive TEG system and be widely adopted to perform the optimization of heat exchanger structures. Liu et al. [16] utilized the CFD model to optimize the thermal and pressure performance of heat exchangers in an automotive TEG system. Through a multi-objective optimization, the temperature uniformity was effectively improved and the pressure drop was decreased. Based on CFD simulations, thermal-electric numerical simulations, and theoretical modelling, Massaguer et al. [17] proposed a new method to evaluate the fuel economy of a TEG system used in automobiles. The results showed that a maximum fuel economy value of 0.18% was predicted for the presented TEG system. To avoid overheating of TEMs, Pacheco et al. [18] integrated variable conductance heat pipes into a novel heat exchanger to control the heat side temperature. Through the established mathematical model, an average power of 572 W for the

TEG system was predicted during a driving cycle, and the model results were partially verified by CFD simulations.

However, both analytical and CFD models can not precisely work out the electric outputs of automotive TEG systems, though with a non-negligible error [19, 20]. Thermal-electric multiphysics numerical models [21, 22] have been developed as a powerful tool to predict the behaviour of thermoelectric devices and can be combined with the CFD model to form a fluid-thermal-electric multiphysics model. Taking the temperature distributions solved by the CFD model as the boundary conditions of the thermal-electric numerical model, the authors [23] performed the modelling of the TEG system containing only one TEM by first considering the fluid-thermal-electric multiphysics field coupling effects. Subsequently, the model was extended to the TEG system containing multiple TEMs with consideration of the topological electric connection among TEMs [24]. In their studies, the influence of parasitic heat such as Joule heat, Peltier heat, and Thomson heat, caused by the electric field on the CFD model is ignored. It is more reasonable to calculate the fluid, thermal, and electric fields at the same time and take into account the multiphysics coupling effects.

All the above models are based on a steady state, but the exhaust temperature and mass flow rate vary with the vehicle speed at any time. Therefore, the theoretical models have to be extended from a steady state into a transient state to investigate the dynamic performance of automotive TEG systems. At present, there is no research report on the transient numerical model of automotive TEG systems, and most current studies use experimental methods to study their transient behaviours. Sponsored by the U.S. Department of Energy, Crane et al. [25] designed a high-temperature TEG system and integrated it into a BMW six-cylinder engine test bench and two passenger vehicles (a BMW X6 and a Lincoln MKT) to perform a bench test and a vehicle test, respectively. The test results of the engine dynamometer showed that the maximum power was more than 500 W under the US06 driving cycle, and the output power of 605 W was reached under the vehicle speed of 125 kph according to on-vehicle tests. Massaguer et al. [26] fabricated an automotive TEG system with 12 TEMs and studied its performance under the transient new European driving cycle (NEDC) and different steady-state engine conditions. They reported that the produced energy of the automotive TEG system under NEDC transient cycle was significantly less than that expected in steady-state conditions. Lan et al. [27] proposed a 2-D analytical model to simulate the dynamic performance of a TEG system prototype, and simulation results of steady-state points were verified by experimental results from a diesel engine test. Nevertheless, as well known, analytical models will predict more unreasonable results than numerical models [19, 28], especially for the automotive TEG system where the complex multiphysics coupling

field effects of the fluid, thermal, and electric fields are involved.

Table 1 summarizes the latest development of theoretical models for thermoelectric devices. It shows that a large number of theoretical models of TEG units or modules have been established, from 1-D to 3-D and from steady state to transient state. However, when the TEG module is used to recover fluid waste heat, especially automotive exhaust heat, there is no comprehensive transient state model to evaluate the dynamic performance of automotive TEG systems. A transient thermal resistance model of the automotive TEG system [27] was thus proposed, with discrete data at different time points as boundary conditions. Nevertheless, the thermal resistance model has numerous simplifications and assumptions, and the physical field distribution characteristics of the TEG system can not be obtained. Considering the high accuracy of the fluid-thermal-electric multiphysics field coupled numerical model, it is attractive to develop a transient multiphysics numerical model.

Table 1. Recent advances of theoretical models for thermoelectric devices and systems.

Research objective	Model type	Features	Steady/transient state	Sources
TEG unit	thermal resistance model	• 1-D • short calculation time • analytical results	steady state transient state	[29] [30]
	thermal-electric numerical model	• from 1-D to 3-D • short calculation time • physical field distributions (thermal and electric fields)	steady state transient state	[31] [32, 33]
	analogy model	• 1-D • short calculation time • analytical results	steady state transient state	[34] [35]
TEG module	thermal resistance model	• 1-D • short calculation time • analytical results	steady state transient state	[36] [30]
	thermal-electric numerical model	• from 1-D to 3-D • relatively long calculation time • physical field distributions (thermal and electric fields)	steady state transient state	[37] [38]
	analogy model	• 1-D • short calculation time • analytical results	steady state transient state	[34] [39]
TEG system for exhaust waste heat recovery	thermal resistance model	• from 1-D to 2-D • short calculation time • analytical results • numerous simplifications and assumptions	steady state transient state	[40] [27]
	CFD model	• 3D • relatively long calculation time • physical field distributions (fluid and thermal fields) • relatively fewer simplifications and assumptions	steady state	[41]
	CFD model combined with	• 3D • relatively long calculation time	steady state	[42]

thermal resistance model	• physical field distributions (fluid and thermal fields) • relatively fewer simplifications and assumptions		
CFD model combined with thermal-electric numerical model	• 3D • relatively long calculation time • physical field distributions (fluid, thermal and electric fields) • few simplifications and assumptions	steady state	[17]
Fluid-thermal-electric multiphysics field coupled numerical model	• 3D • long calculation time • physical field distributions (fluid, thermal and electric fields) • almost no simplifications and assumptions	steady state	[24, 43]

Therefore, this work is intended to improve the fluid-thermal-electric multiphysics numerical model and extend it from a steady-state into a transient state. Based on a simplified TEG system used for automotive exhaust waste heat recovery, a transient fluid-thermal-electric multiphysics coupling field numerical model is proposed for the first time, and the dynamic performance is investigated under the Economic Commission for Europe (ECE) driving cycles. The presented model takes the dynamic characteristics, fluid-thermal-electric multiphysics field coupling effects, material temperature dependence, and other factors into consideration, making it thus far the most complete model ever, and it can be used to predict the dynamic performance of automotive TEG systems under real conditions. Section 2 describes the details of the transient fluid-thermal-electric multiphysics coupling field numerical model, including governing equations and boundary conditions. Section 3 validates the model through grid independence examination and experimental results in a transient-state condition. Section 4 analyzes the dynamic performance under ECE driving cycles. The main findings of this work are summarized in Section 5.

2. Transient fluid-thermal-electric multiphysics coupling field numerical model

In this work, a simplified automotive thermoelectric generator (TEG) system containing one thermoelectric module (TEM) was taken as the research object, and the dynamic performance of the TEG system under transient automobile driving cycles was analyzed via the proposed transient fluid-thermal-electric multiphysics coupling field numerical model. In a practical situation, the automotive TEG system should contain a series of TEMs to generate considerable electric energy, but this means a huge workload, which requires considerable computing power and time to perform the transient numerical simulations. In future work, the dynamic performance analysis will be extended from the simplified automotive TEG system to a comprehensive automotive TEG system. Detailed features of

the simplified automotive TEG system are described in Section 2.1, and details about the transient fluid-thermal-electric multiphysics coupling field numerical model are elucidated in the next subsections.

2.1 A simplified thermoelectric generator system used to recover automotive exhaust waste heat

The geometry and configuration of the simplified automotive TEG system are shown in Fig. 1. When recycling the waste heat from automotive exhaust gases, a heat exchanger is required to absorb the heat contained in hot fluids and supply heat for TEMs. Generally, the heat transfer performance of the heat exchanger determines the output performance of the whole TEG system to a large extent. Therefore, some fin structures are attached on the inner hot side surfaces of the heat exchanger to increase the convective heat transfer area and the hot side temperature, as shown in Fig. 1(b). In addition, a cooling device was arranged on the cold side of the TEM to dissipate the heat. Automotive exhaust gases and cooling water flow through the heat exchanger and cooling device, respectively. The TEM is sandwiched between the heat exchanger and the cooling device, and it will generate electric energy under the action of temperature difference. The overall schematic of the TEG system is shown in Fig. 1(a). Here, both heat exchanger and cooling device are made of aluminum materials, and two steel connectors are connected to the heat exchanger as the exhaust inlet and outlet. The pipeline diameters of the exhaust channel and coolant channel are 40 mm and 5.5 mm, respectively. The TEM (TEG-127020, P&N technology, China) consists of 128 pairs of Bi_2Te_3-based p-type and n-type thermoelectric legs, 256 copper electrodes, and 2 ceramic plates. The sizes of the thermoelectric leg, copper electrode, load resistance, and ceramic plate are 1.4×1.4×1.0 (Length×Width×Height) mm^3, 3.8×1.4×0.35 (Length×Width×Height) mm^3, 0.5×0.5×35.5 (Length×Width×Height) mm^3, and 40×44 (and 40)×0.8 (Length×Width×Height) mm^3, respectively. Detailed material properties of the TEG system are listed in Table 2.

Table 2. Detailed material properties of the simplified automotive TEG system

Component name	Material name	Material properties	Value	Unit
p-type thermoelectric legs	p-type Bi_2Te_3	Thermal conductivity	$-3.0595\times10^{-9}T^4+4.5678\times10^{-6}T^3$ $-2.5162\times10^{-3}T^2+0.6107T-53.9863$	W/(m·K)
		Electrical resistivity	$-3.088\times10^{-9}T^4+4.5653\times10^{-6}T^3$ $-2.5854\times10^{-3}T^2+0.6558T-60.588$	10^{-5} Ω·m
		Seebeck coefficient	$-1.8027\times10^{-7}T^4+3.2363\times10^{-4}T^3$ $-0.2154T^2+62.9744T-6616.5678$	μV·K^{-1}
		Specific heat capacity	188	J/(kg·K)
		Density	6600	kg/m^3
n-type thermoelectric	n-type Bi_2Te_3	Thermal conductivity	$-3.0595\times10^{-9}T^4+4.5678\times10^{-6}T^3$ $-2.5162\times10^{-3}T^2+0.6107T-53.9863$	W/(m·K)

legs		Electrical resistivity	$-3.088\times10^{-9}T^4+4.5653\times10^{-6}T^3$ $-2.5854\times10^{-3}T^2+0.6558T-60.588$	10^{-5} Ω·m
		Seebeck coefficient	$1.8027\times10^{-7}T^4-3.2363\times10^{-4}T^3$ $+0.2154T^2-62.9744T+6616.5678$	μV·K^{-1}
		Specific heat capacity	188	J/(kg·K)
		Density	6600	kg/m^3
Copper electrodes	Copper	Thermal conductivity	165.64	W/(m·K)
		Electrical resistivity	1.75×10^{-3}	10^{-5} Ω·m
		Specific heat capacity	381	J/(kg·K)
		Density	8978	kg/m^3
Load resistance	-	Thermal conductivity	400	W/(m·K)
		Electrical resistivity	3.52~70.4	10^{-5} Ω·m
		Specific heat capacity	381	J/(kg·K)
		Density	8978	kg/m^3
Ceramic plates	Alumina ceramic	Thermal conductivity	22	W/(m·K)
		Specific heat capacity	850	J/(kg·K)
		Density	3600	kg/m^3
Heat exchanger and cooling device	Aluminum	Thermal conductivity	217.7	W/(m·K)
		Specific heat capacity	871	J/(kg·K)
		Density	2719	kg/m^3
Steel connectors	Steel	Thermal conductivity	17	W/(m·K)
		Specific heat capacity	502.48	J/(kg·K)
		Density	8030	kg/m^3

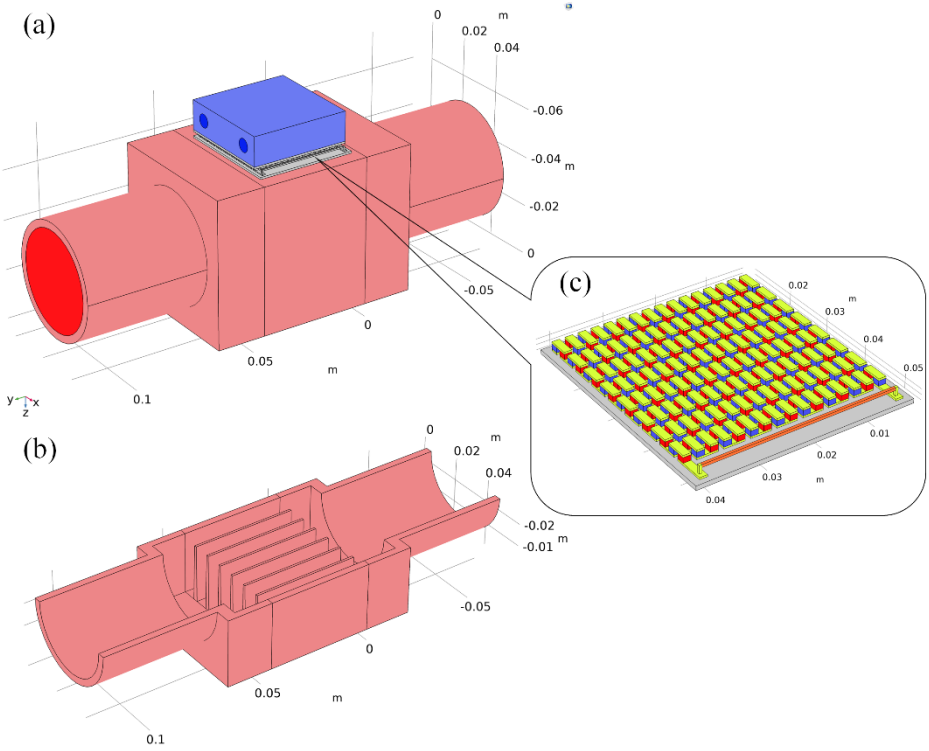

Fig.1. Diagram of the simplified TEG system used to recover automotive exhaust waste heat. (a) Overall schematic of the TEG system. (b) Sectional view of the heat exchanger structure. (c) Schematic of the TEM structure.

2.2 Governing equations

The transient fluid-thermal-electric multiphysics coupling field numerical model proposed in this

work is based on the following assumptions and simplifications:

(i) Owing to its negligible influence, the thermal resistance between TEM and heat exchanger (or cooling device) is ignored.

(ii) Thermoelectric materials are isotropic.

(iii) Air is taken as exhaust gas and water is taken as coolant.

The governing equations of the transient fluid-thermal-electric multiphysics coupling field numerical model can be classified into two parts: conservation equations of the fluid region and solid region. Since the Mach numbers of exhaust gas and cooling water are quite low, the fluid flow can be regarded as incompressible [44], which has almost no effect on the model accuracy. The governing equations of mass, momentum, and energy for the incompressible and transient-state fluid flow in the exhaust gas channel and cooling water channel can be expressed as follows:

$$\nabla \cdot \left(\rho \vec{v} \right) = 0 \tag{1}$$

$$\frac{\partial}{\partial t}\left(\rho \vec{v} \right) + \nabla \cdot \left(\rho \vec{v} \vec{v} \right) = -\nabla p + \nabla \cdot \left[\mu \left(\nabla \vec{v} + \nabla \vec{v}^{T} \right) \right] \tag{2}$$

$$\rho c \frac{\partial T}{\partial t} + \rho c \vec{v} \cdot \nabla T - \nabla \cdot \left(\lambda \nabla T \right) = 0 \tag{3}$$

where ρ, t, $\vec{v}$, μ, c, T, and λ represent the density, time, fluid velocity vector, dynamic viscosity, specific heat capacity, temperature, and thermal conductivity of exhaust gas and cooling water, respectively. In this study, the air material properties are used as the material properties of exhaust gases, and the temperature dependences of both air and water are taken into consideration.

The k-ε model is also used to simulate the turbulent flow. The turbulent kinetic energy k and its rate of dissipation ε are computed by the following transportation equations:

$$\frac{\partial}{\partial t}\left(\rho k \right) + \frac{\partial}{\partial x_i}\left(\rho k u_i \right) = \frac{\partial}{\partial x_j}\left[\left(\mu + \frac{\mu_t}{\sigma_k} \right) \frac{\partial k}{\partial x_j} \right] + G_k + G_b - \rho \varepsilon \tag{4}$$

$$\frac{\partial}{\partial t}\left(\rho \varepsilon \right) + \frac{\partial}{\partial x_i}\left(\rho \varepsilon u_i \right) = \frac{\partial}{\partial x_j}\left[\left(\mu + \frac{\mu_t}{\sigma_\varepsilon} \right) \frac{\partial \varepsilon}{\partial x_j} \right] + C_{1\varepsilon} \frac{\varepsilon}{k}\left(G_k + C_{3\varepsilon} G_b \right) - C_{2\varepsilon} \rho \frac{\varepsilon^2}{k} \tag{5}$$

with

$$\mu_t = \rho C_\mu \frac{k^2}{\varepsilon} \tag{6}$$

where, G_k is the generation of turbulent kinetic energy due to the mean velocity gradients, G_b is the generation of turbulent kinetic energy due to buoyancy and, σ_k and σ_ε are the turbulent Prandtl numbers for k and ε, respectively. $C_{1\varepsilon}$, $C_{2\varepsilon}$, $C_{3\varepsilon}$, and C_μ are constants.

The fluid-thermal multiphysics coupling field in fluid regions can be characterized by Eqs (1)-(6). As for the thermal-electric multiphysics coupling field in solid regions, including aluminum, steel, ceramic, copper, load resistance, p-type and n-type thermoelectric materials, the transient-state energy conservation can be defined as:

$$\left(\rho c\right)_{\mathrm{m}} \frac{\partial T}{\partial t} = \nabla \cdot \left(\lambda_{\mathrm{m}} \nabla T\right) + \dot{S}_{\mathrm{m}} \tag{7}$$

where ρ, c, and λ represent the density, specific heat capacity, and thermal conductivity of solid materials, respectively. Subscript m denotes different materials, al for aluminum, st for steel, ce for ceramic, co for copper, L for load resistance, p for the p-type thermoelectric material, and n for the n-type thermoelectric material, respectively. Noted that $\lambda_{\mathrm{p}}(T)$ and $\lambda_{\mathrm{n}}(T)$ are temperature-dependent. The first term on the left side represents the change of internal energy, the first term on the right side represents the Fourier heat conduction, and $\dot{S}_{\mathrm{m}}$ is the energy source term. In p-type and n-type thermoelectric material regions, the energy source term includes Joule heat and Thomson heat while it is absent in the aluminum, steel, and ceramic regions:

$$\dot{S}_{\mathrm{m}} = \begin{cases} \sigma_{\mathrm{p}}^{-1}\left(T\right)\vec{J}^{2} - \nabla\alpha_{\mathrm{p}}\left(T\right)\vec{J}T_{\mathrm{p}}; & \text{p-type thermoelectric unit} \\ \sigma_{\mathrm{n}}^{-1}\left(T\right)\vec{J}^{2} - \nabla\alpha_{\mathrm{n}}\left(T\right)\vec{J}T_{\mathrm{n}}; & \text{n-type thermoelectric unit} \\ \sigma_{\mathrm{co}}^{-1}\vec{J}^{2}; & \text{copper} \\ \sigma_{\mathrm{L}}^{-1}\vec{J}^{2} & \text{load resistance} \\ 0; & \text{aluminum, steel, ceramic} \end{cases} \tag{8}$$

where $\sigma_{\mathrm{p}}^{-1}\left(T\right)$, $\sigma_{\mathrm{n}}^{-1}\left(T\right)$, $\sigma_{\mathrm{co}}^{-1}$, and σ_{L}^{-1} are the electrical resistivities of the p-type thermoelectric unit, n-type thermoelectric unit, copper, and load resistance, respectively. $\alpha_{\mathrm{p}}(T)$ and $\alpha_{\mathrm{n}}(T)$ are the Seebeck coefficients of the p-type and n-type thermoelectric units, respectively. $\vec{J}$ is the current density vector.

In the electric field, the conservation equations include:

$$\vec{E} = -\nabla\phi + \alpha_{\mathrm{p,\,n}}\left(T\right)\nabla T \tag{9}$$

$$\vec{J} = \sigma_{\mathrm{m}}\vec{E} \tag{10}$$

$$\nabla \cdot \vec{J} = 0 \tag{11}$$

where, $\vec{E}$ is the electric field vector, ϕ is the electric potential, $\alpha_{\mathrm{p,n}}\left(T\right)\nabla T$ is the Seebeck voltage, σ_{m} represents the electrical conductivity of the p-type unit ($\sigma_{\mathrm{p}}(T)$), n-type unit ($\sigma_{\mathrm{n}}(T)$), and copper (σ_{co}). Eq. (11) denotes the continuity of the electric current.

2.3 Boundary conditions

The governing equations mentioned above have completed the modelling of the transient multiphysics coupling field of the fluid, thermal, and electric fields of the TEG system. In this work, the transient fluid-thermal-electric multiphysics coupling field numerical model was established on the platform of COMSOL Multiphysics 5.4, and the fluid, thermal, and electric fields were calculated at the same time. To compute the above equations, specific boundary conditions should be given, including inlet and outlet boundary conditions of fluid flow, heat transfer boundary conditions, and electric boundary conditions. Detailed settings of the boundary conditions of the TEG system are shown in Fig. 2, where A and D are the respective inlet and outlet boundary conditions of the exhaust channel, B and C are the respective inlet and outlet boundary conditions of the coolant channel, E is the natural heat transfer boundary condition, and F is the grounded boundary condition.

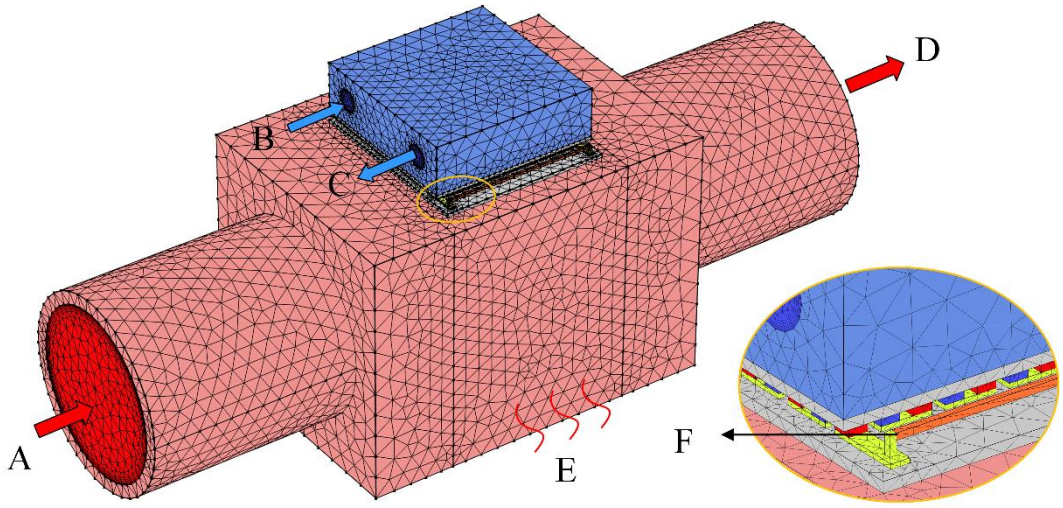

Fig. 2. Finite element model and boundary conditions of the simplified TEG system used to recover automotive exhaust waste heat. A: inlet boundary of exhaust gases, B: inlet boundary of cooling water, C: outlet boundary of cooling water, D: outlet boundary of exhaust gases, E: natural heat transfer boundary, F: grounded boundary.

Exhaust gases enter the channel of the heat exchanger at a transient temperature of $T_{ex}(t)$ and a transient mass flow rate of $\dot{m}_{ex}(t)$ while cooling water enters the channel of the cooling device at a constant temperature of 300 K and a constant velocity of 10 m/s. Both exhaust gases and cooling water leave the channels at constant standard atmosphere pressure. For the surfaces exposed to the external environment, a natural convective heat transfer boundary condition is defined as follows:

$$-\lambda \frac{\partial T}{\partial n} = h_{\text{ext}} \left(T - T_{\text{ext}} \right) \tag{12}$$

where h_{ext} = 15 W·m^{-2}·K^{-1} is the external convective heat transfer coefficient, and T_{ext} = 300 K is the

external temperature. Furthermore, a grounded boundary condition is defined on the contact terminal between load resistance and TEM, marked as F in Fig. 2, in which the electric potential is equal to 0 V.

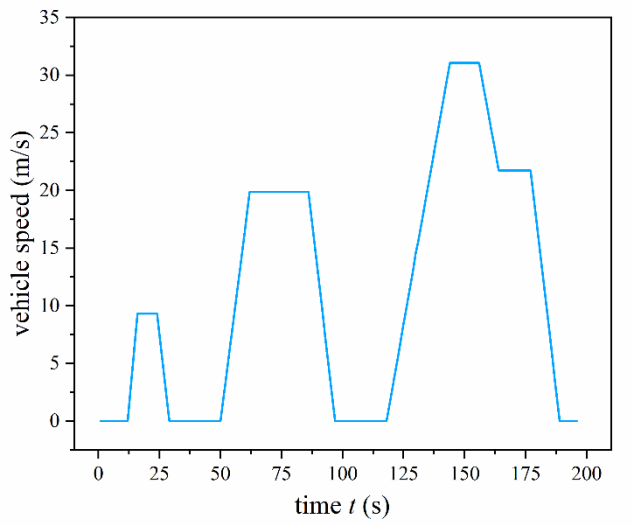

Fig. 3. Vehicle speed under one ECE cycle.

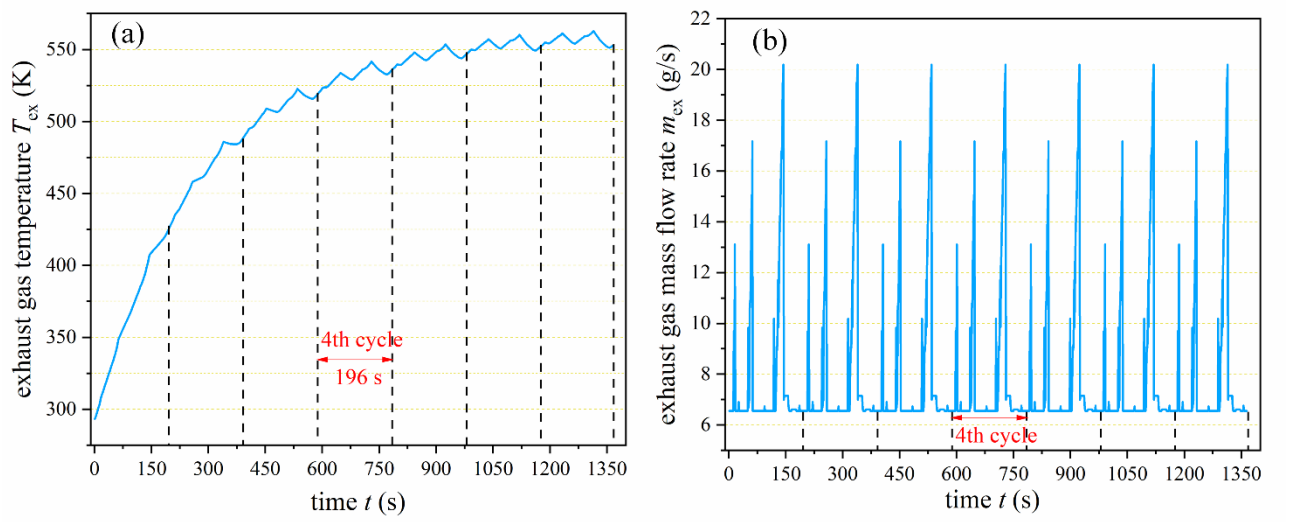

Fig. 4. Exhaust temperature $T_{ex}(t)$ and exhaust mass flow rate $\dot{m}_{ex}(t)$ under seven ECE cycles.

In practical application, both $T_{ex}(t)$ and $\dot{m}_{ex}(t)$ change with the change of vehicle speed. In this study, the ECE driving cycle of the Economic Commission for Europe (ECE) cycle is selected to study the dynamic performance of the TEG system. Fig. 3 shows the vehicle speed under one ECE cycle, and the period of each ECE cycle is 196 s. To obtain the transient characteristics of exhaust temperature and mass flow rate under ECE cycles, the vehicle simulation software of ADVISOR 2003 was used to simulate the real operation of the vehicle under ECE driving conditions. In the platform of ADVISOR, a VEH_SMCAR conventional vehicle with a 3.0 L, 6-cylinder gasoline engine was selected, and the

maximum engine power was 102 kW. After the settings of the given conventional vehicle, both temperature and mass flow rate of exhaust gases under seven ECE cycles were obtained, as shown in Fig. 4. Here, the exhaust gas temperature fluctuates from 273.15 K to 550 K because the initial temperature of the automobile exhaust system is 273.15 K and is gradually heated by the high-temperature exhaust gases. The fluctuation of exhaust temperature is caused by the variation of exhaust mass flow rate. In a considerable time, the exhaust gas mass flow rate is at the minimum value of 6.55 g/s. The changing trend of exhaust mass flow rate and vehicle speed in each ECE cycle is similar because the vehicle will consume more fuel and generate more exhaust gases when accelerating, and vice versa. The simulated transient temperature and mass flow rate were used as the inlet boundary conditions of the transient numerical model.

2.4 Definition of performance parameters

Output voltage, output power, and conversion efficiency are commonly used parameters to evaluate the performance of the TEG system. Here, the output voltage (U_L) of the TEG system is defined as the electric potential difference of the load resistance (R_L), and the corresponding output power is expressed as:

$$P(t)=\frac{U_L^2(t)}{R_L} \tag{13}$$

Furthermore, the conversion efficiency of the TEG system is defined as:

$$\eta(t)=\frac{P(t)}{Q_h(t)} \tag{14}$$

with

$$Q_h(t)=c\dot{m}_{ex}(t)\left[T_{ex}(t)-T_{out}(t)\right] \tag{15}$$

where $Q_h(t)$ is the transient heat absorption of the TEG system. $T_{out}(t)$ is the transient exhaust temperature at the outlet surface of the heat exchanger, which is extracted from numerical results.

3. Model validation

3.1 Grid independence verification

The finite element model of the TEG system is shown in Fig. 2. The grid of different regions was controlled by their specific physical fields. For instance, the boundary layer mesh with five layers was defined on the contact walls of fluid regions with solid regions to accurately simulate the turbulent

flow. To test the grid independence, the grid system of the TEG system was set to different grid sizes, and four grid systems with grid numbers of 5645539, 1505248, 454702, and 195023 were designated as grids I, II, III, and IV, respectively. To save on execution time, the grid independence verification was conducted under steady-state working conditions, where average exhaust temperature and average exhaust mass flow rate of seven ECE cycles were used as the inlet boundary conditions. Through a simple calculation, the average exhaust temperature is 503.79 K, and the average exhaust mass flow rate is 7.73 g/s. The output performance of the TEG system for the four grid systems with a load resistance of 4 Ω is listed in Table 3. Note that the model accuracy increases with the increasing grid number. To reduce the workload and ensure sufficient accuracy of the numerical model, grid II was selected for the transient numerical simulations in the following sections.

Table 3. Output voltage and output power of the TEG system for the four grid systems with a load resistance of 4 Ω.

	Grid number	Output voltage (V)	Output power (W)	Error of voltage	Error of power
Grid I	5645539	2.3112	1.3354	0	0
Grid II	1505248	2.3149	1.3397	0.16%	0.32%
Grid III	454702	2.3286	1.3556	0.75%	1.51%
Grid IV	195023	2.3515	1.3824	1.74%	3.52%

3.2 Experimental verification

To validate the accuracy of the proposed transient fluid-thermal-electric multiphysics coupling field numerical model, a test bench was designed to measure the dynamic output performance of the TEG system under transient working conditions, as shown in Fig. 5. To eliminate the air gap between TEM and heat exchanger (or cooling device), thermal grease was evenly applied on both sides of TEM, and the whole TEG system structure was clamped together by a clamping device. Tap water flowed through the cooling device of the TEG system to dissipate the heat of TEM. The temperature and mass flow rate of tap water are 284.85 K and 21.19 g/s respectively. An air heater (F1-R1055, FTV, China) with a maximum power of 5 kW was used to provide a heat source for the TEG system. Dynamic air temperature and air flow rate were generated by turning knobs on the air heater. K-type thermal sensors (WRNT, Huarun, China) were placed in the inlet and outlet connectors of the TEG system to measure the inlet and outlet air temperatures, respectively. A temperature data logger (RDXL4SD, OMEGA, US) with an accuracy of ±0.4% was used to read and record the data of thermal sensors. An electronic load (IT8500+, ITECH, China) was connected with the TEG system to form a complete circuit. The load resistance was set to 4 Ω. To record the transient voltage data, an oscilloscope (DS1074, RIGOL, China) was connected to the electronic load. A hot-wire anemometer (HHF-SD1, OMEGA, US), with

an accuracy of ±5%, was used to measure the transient air velocity data. The hot-wire anemometer consists of an air velocity sensor and an air velocity data logger. The air velocity sensor was installed in the pipe behind the TEG system. However, the working temperature of the air velocity sensor should not exceed 50 ℃. Consequently, an air cooler was placed between the TEG system and the pipe where the air velocity sensor was located, which was powered by a DC power supply (UTP1305, UNI-T, China). The air velocity was also controlled in a small range to avoid damaging the air velocity sensor.

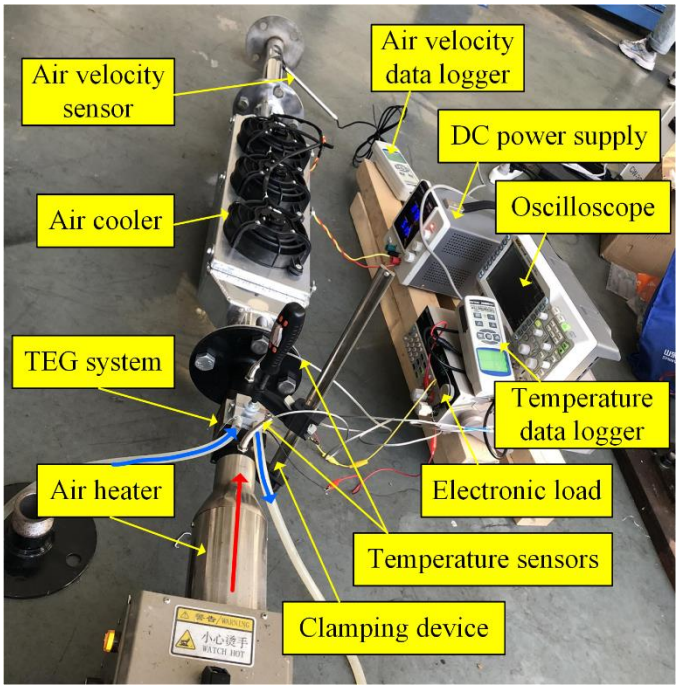

Fig. 5. Transient performance test bench of the TEG system.

The air temperature and air velocity change instantaneously by turning the air heater knobs. The corresponding data of transient air temperature and transient air velocity were obtained and used as the transient inlet air boundary conditions of the transient fluid-thermal-electric multiphysics coupling field numerical model. Fig. 6 shows the comparison of transient output voltage between numerical and experimental results under transient heat source inputs. The output voltage predicted by the transient numerical model fluctuated more smoothly than that obtained by experimental tests. The average deviation of transient output voltage between numerical and experimental results is 9.24%. On the one hand, the measurement error of instruments is responsible for the deviation of the output voltage. On the other hand, the temperature of the thermal sensor probe will not change instantaneously due to its thermal inertia, but this factor can not be taken into account in the transient numerical model. Considering the error of transient experiments, the deviation of the transient output voltage is acceptable.

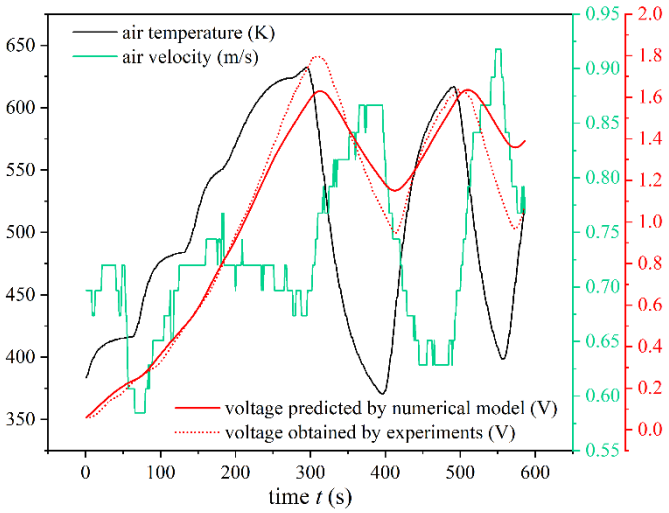

Fig. 6. Comparison of transient output voltage between numerical results and experimental results.

4. Results and discussion

In this section, with the average exhaust temperature (503.79 K) and average exhaust mass flow rate (7.73 g/s) of seven ECE cycles taken as the boundary conditions, the physical field distribution characteristics of the TEG system were obtained by solving the above model. Next, the steady-state performance of the TEG system was studied, and the maximum power point of the TEG system was obtained. Furthermore, the transient-state performance analysis of the TEG system at the maximum power point was conducted, including the transient output voltage, output power, and conversion efficiency. Finally, a comparison of output power between steady-state and transient-state analysis was performed.

4.1 Physical field distribution characteristics of the thermoelectric generator system

Fig. 7 shows the temperature distributions of the TEG system. The temperature at the hot side of the heat exchanger is seen to be about 100 K lower than the inlet exhaust temperature, whereas the temperature of the cooling device is very close to that of cooling water. The reason for this is that the specific heat capacity and flow rate of exhaust gases are obviously lower than those of cooling water. According to the temperature distributions of the sectional surfaces in Fig. 7 (b), there is a temperature drop of exhaust gases from inlet to outlet, because part of the heat contained in exhaust gases is taken away by the cooling water or converted into electricity. Additionally, the temperature of exhaust gases in the chamber of the heat exchanger is lower than that in the channels of inlet and outlet connectors owing to the bigger volume of the chamber of the heat exchanger. Driven by the temperature

difference, the carriers of thermoelectric materials will move from the high-temperature to the low-temperature side so that a Seebeck voltage is generated.

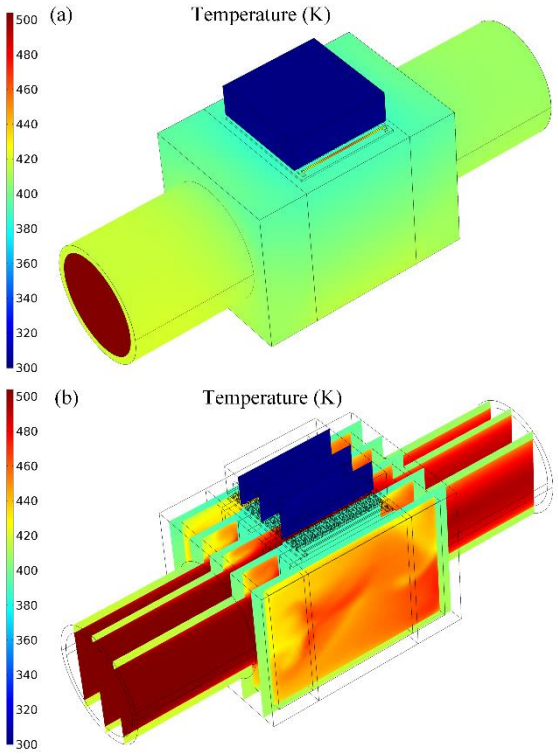

Fig. 7. Temperature distributions of (a) the whole TEG system and (b) five sections.

Fig. 8 (a) shows the voltage distributions of the TEG system. The electric voltage only exists along the thermoelectric legs, copper electrodes, and load resistance, because the electric field governing equations are absent in other regions. Further details about the voltage distributions of the TEM can be found in Fig. 8 (b). As can be seen, the electric potential of TEM increases with the number of thermoelectric legs in series, and the output voltage equals the electric potential difference of the TEM. It seems that the output power of TEM can be enhanced by increasing the number of thermoelectric legs. Fig. 8 (c) shows the current density distributions of the TEM. The absolute value of the current density in copper electrodes is the highest due to the lowest electric resistivity and the smallest cross-sectional area of copper electrodes. The current density of two adjacent rows of copper electrodes is opposite because of the opposite direction of the electric current. The temperature distributions of the TEM are shown in Fig. 8 (d). The temperature of load resistance is the highest due to the Joule effect. From the hot end to the cold end of TEM, due to the low thermal conductivity of thermoelectric materials, there is a large temperature drop along thermoelectric legs. Generally, the lower the thermal conductivity of thermoelectric materials is, the higher the temperature difference between two sides of thermoelectric legs will be, thereby resulting in greater output performance.

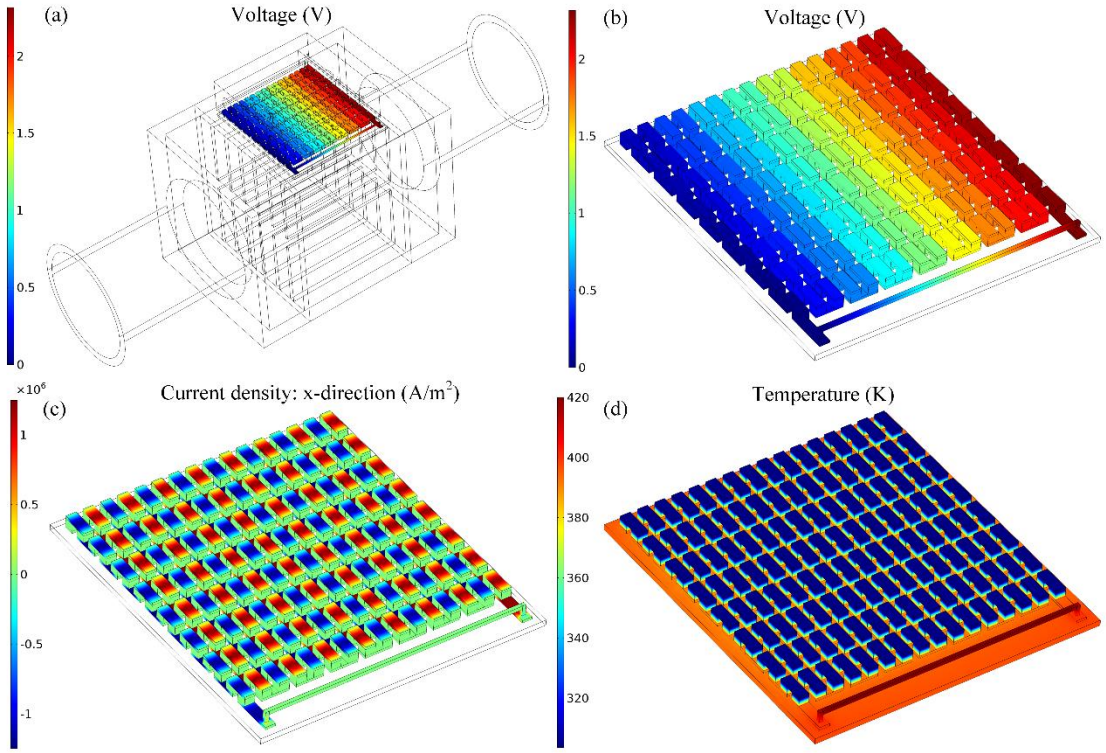

Fig. 8. Numerical results of the TEG system. (a) Voltage distributions of the TEG system. (b) Detailed voltage distributions of the TEM. (c) Current density distributions of the TEM. (d) Temperature distributions of the TEM.

4.2 Steady-state performance analysis of the thermoelectric generator system

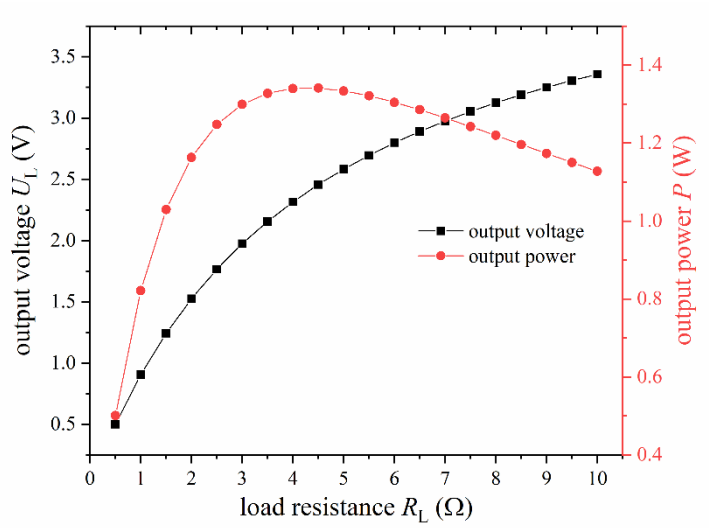

Fig. 9. Output performance of the TEG system using the average exhaust temperature and average exhaust mass flow rate.

Under the boundary conditions of the average exhaust temperature and average exhaust mass flow rate, a steady-state performance analysis of the TEG system was performed. Fig. 9 shows the output performance of the TEG system under different load resistances. Like a common circuit, as the load resistance increases, the output voltage will increase. However, with the increase of load resistance,

the output power increases first and then decreases. When the load resistance is about 4 Ω, the TEG system reaches the highest output power, that is 1.34 W. As mentioned above, one of the main purposes of the steady-state performance analysis is to determine the maximum power point so as to study the transient performance of the TEG system at driving cycles. Therefore, the maximum power point of R_L = 4 Ω was selected for the transient numerical simulations.

4.3 Transient-state performance of the thermoelectric generator system under ECE driving cycles

4.3.1 Output voltage and output power

Fig. 10 shows the output voltage and output power of the TEG system under seven ECE cycles. Over time, both voltage and power increase, because the heat exchanger of the TEG system is gradually heated by exhaust gases from an initial temperature of 300 K and then reaches equilibrium. Output power is computed according to the data of output voltage, and thus, the variation of output power shows the same trend with that of output voltage but with greater amplitude. The total generated electric energy of the TEG system of seven ECE cycles is 1624.07 J. Combined with Fig. 4, the fluctuation of output performance is a result of the transient change of exhaust temperature and exhaust mass flow rate. However, the convex parts of the output performance curves are more obvious than those of the exhaust temperature curve, though much smoother than those of the exhaust mass flow rate. To further analyze the dynamic response characteristics of the TEG system, the output power and output power in the second and seventh ECE cycles are obtained.

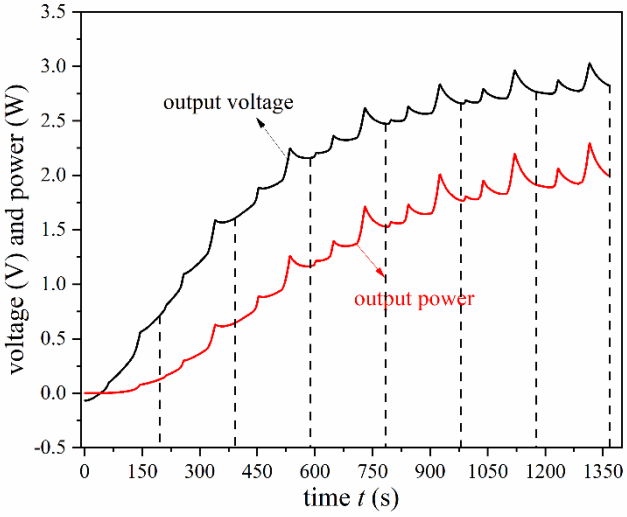

Fig. 10. Output voltage and output power of the TEG system under seven ECE cycles.

The output performance of the TEG system under the second and seventh ECE cycles is shown in Figs 11 (a) and (b), respectively. As can be seen, the exhaust temperature is directly related to the

exhaust mass flow rate. When the exhaust mass flow rate changes rapidly, the inflection points appear in the exhaust temperature curve, as well as in the curves of output voltage and output power. In an ECE cycle, there are three parts where the exhaust mass flow rate changes rapidly, named parts I, II, and III, respectively. Part I is close to the beginning of an ECE cycle while part III is close to the end of an ECE cycle. The periods for parts I, II, and III are about 5 s, 13 s, and 27 s, respectively, and the variation amplitudes from the lowest mass flow rate to the highest one for parts I, II, and III are 6.56 g/s, 10.62 g/s, and 13.64 g/s, respectively. According to the figures, the change of output voltage and output power is smoother than that of exhaust temperature and mass flow rate, especially the exhaust mass flow rate. Nevertheless, in the steady-state numerical simulation, the output performance of the TEG system changes with the change of the exhaust inlet boundary conditions, which means there is a great deviation between steady-state and transient-state performance analysis. According to the data of part I in Figs 11 (a) and (b), it seems that the outputs of the TEG system will not be affected by the small and short-term fluctuations of the exhaust parameters. The reason for this is that the temperature of the TEG system has been in a relatively stable state for a time, the small and short-term temperature fluctuations will not affect this state, and after this fluctuation, the TEG system is heated by new relatively stable exhaust gases.

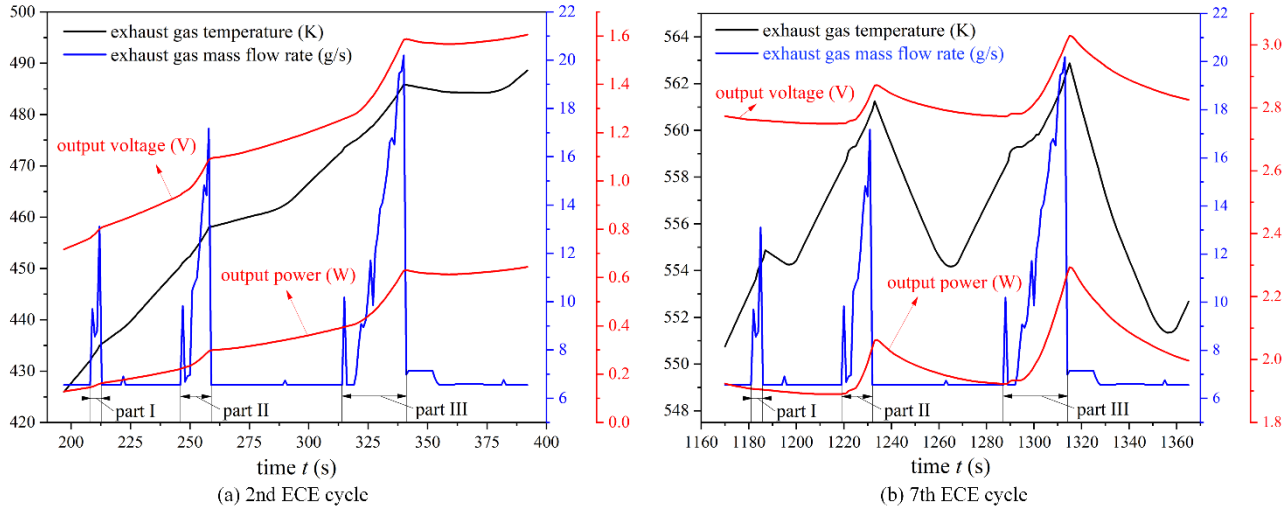

Fig. 11. Output voltage and output power of the TEG system under the (a) second ECE cycle and (b) seventh ECE cycle. Note: The first y-axis denotes the exhaust gas temperature, the second y-axis denotes the exhaust gas mass flow rate, and the third y-axis denotes the output voltage or output power.

When t = 285 s, the temperature of exhaust gases changes from a slow increase to a rapid increase, but the corresponding change of TEG system output from a slow increase to a rapid increase occurs at t = 320 s. Moreover, in the seventh ECE cycle, when t = 1265 s, the temperature of exhaust gases

changes from decreasing to increasing while the corresponding change of TEG system output happens at t = 1290 s. A delay occurs in the output response of the TEG system for a smooth change in exhaust temperature between parts II and III. Although the state of the exhaust temperature is changed, the temperature of the TEG system will remain at the previous state for a period of time before the corresponding change of output voltage and output power of the TEG system. The change of outputs is often accompanied by the change of exhaust mass flow rate as well. The reason the output of the TEG system gradually decreases after part III of the sixth ECE cycle and begins to increase until part II of the seventh ECE cycle can also be explained by the delay of output response and the negligible influence of the small and short-term fluctuation of exhaust gases.

4.3.2 Heat absorption and conversion efficiency

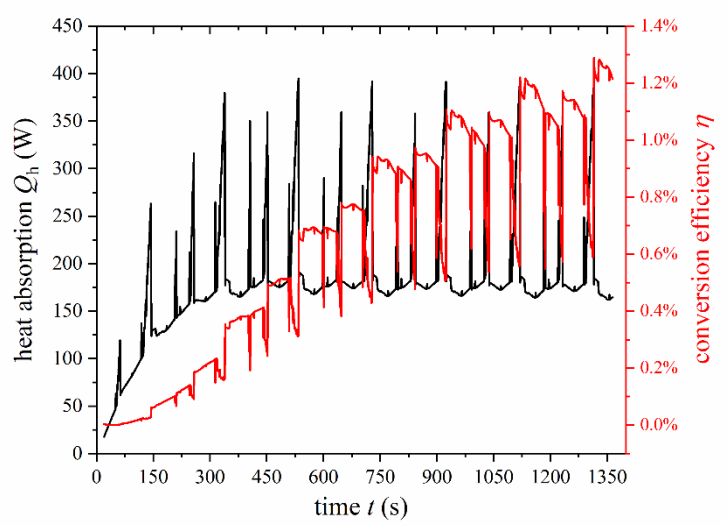

Fig. 12. Heat absorption and conversion efficiency of the TEG system under seven ECE cycles.

The conversion efficiency and heat absorption of the TEG system are calculated by Eqs (14) and (15), respectively, and the calculation results are shown in Fig. 12. When $t \geq 392$ s, that is the end of the second ECE cycle; the heat absorption reaches equilibrium and remains the same trend in the subsequent ECE cycles, which may be caused by the temperature drop (ΔT) from the exhaust inlet to the exhaust outlet, as shown in Fig. 13. The ΔT of the first two ECE cycles is found to increase rapidly and keep almost the same changing trend in the subsequent ECE cycles, thus causing the corresponding change of heat absorption. There are a great number of convexes in the heat absorption curve, but they are represented as concaves in the temperature drop curve. With the increase of exhaust mass flow rate, the heat absorption increases, resulting in convexes of the heat absorption curve. However, for the case of temperature drop, more exhaust gas is used to supply heat for the TEG system, resulting in

a decrease in temperature drop.

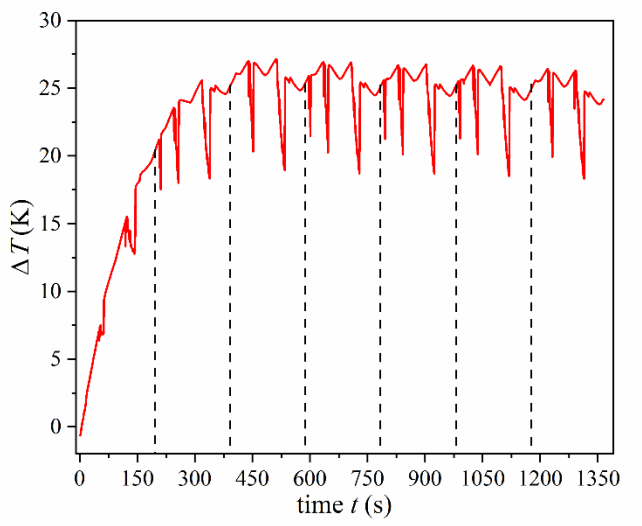

Fig. 13. Temperature drop from the exhaust inlet to the exhaust outlet.

Both heat absorption and conversion efficiency are mainly affected by the exhaust mass flow rate, followed by the exhaust temperature. Nonetheless, the situation of conversion efficiency is quite different from that of heat absorption. Heat absorption is directly proportional to the exhaust mass flow rate, whereas conversion efficiency is inversely proportional to the exhaust mass flow rate. The conversion efficiency of the subsequent ECE cycles is higher than that of the previous ECE cycles, especially for the first three ones. According to the exhaust characteristics in Fig. 4, the temperature change of the vehicle exhaust system will reach equilibrium after seven ECE cycles, which means the conversion efficiency of the TEG system will fluctuate between 0.6% and 1.3%. In the previously developed automotive TEG systems [7, 45], the conversion efficiency is about 2%, and the reason for the low conversion efficiency of this TEG system can be attributed to the low-grade exhaust gases of ECE cycles and the low heat transfer performance of the TEG system. In addition, when the exhaust mass flow rate increases rapidly, the conversion efficiency decreases dramatically, and vice versa.

To further analyze the transient characteristics of the conversion efficiency of the TEG system, detailed heat absorption and conversion efficiency in the 7th ECE cycle are obtained, as shown in Fig. 14. The changing trend of heat absorption is observed to be basically consistent with that of exhaust mass flow rate while the changing trend of conversion efficiency can be regarded as the inverted image of that of exhaust mass flow rate. The influence of exhaust temperature on the conversion efficiency is also far less than that of the exhaust mass flow rate. Compared with the transient characteristics of output voltage and output power in Figs 10 and 11, heat absorption and conversion efficiency show more intense changes and faster responses with the change of exhaust mass flow rate. In summary, the

dynamic response of output voltage and output power is much smoother than the change of exhaust characteristics while the dynamic conversion efficiency mainly depends on the exhaust mass flow rate and presents the opposite changing trend with the exhaust mass flow rate.

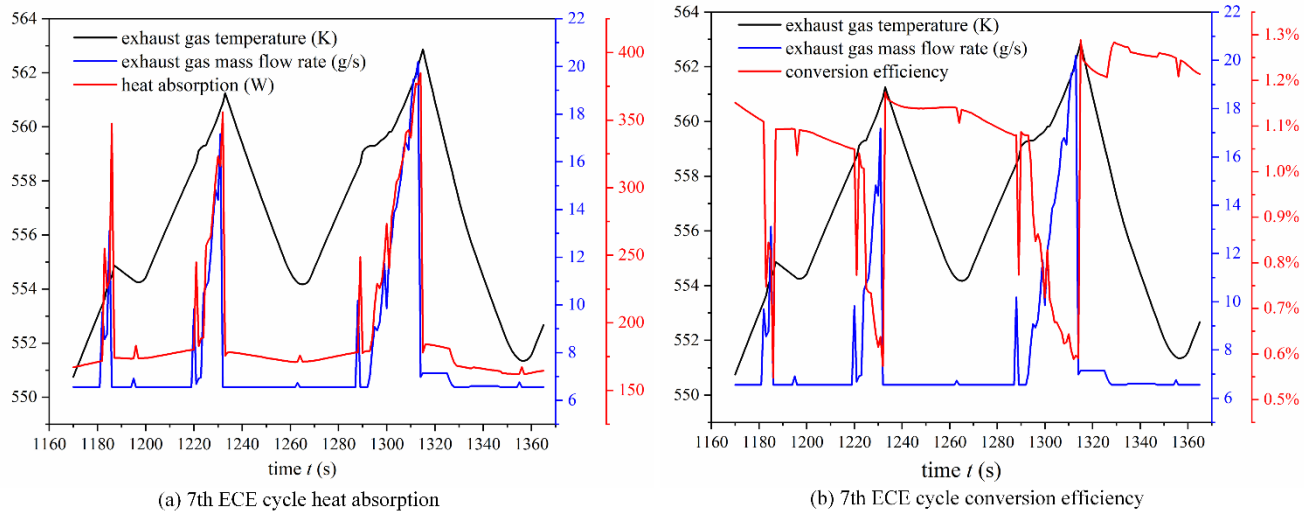

(a) 7th ECE cycle heat absorption (b) 7th ECE cycle conversion efficiency

Fig. 14. Heat absorption and conversion efficiency of the TEG system under the seventh ECE cycle. (a) Heat absorption. (b) Conversion efficiency. Note: The first y-axis denotes the exhaust gas temperature; the second y-axis denotes the exhaust gas mass flow rate, and the third y-axis denotes (a) heat absorption or (b) conversion efficiency.

4.4 Comparison of generated electric energy between steady-state and transient-state analysis

In this paper, the transient numerical analysis of the automotive TEG system is carried out for the first time, whereas the previous studies are based on the steady-state. To investigate the difference of output performance between transient analysis and steady-state analysis, the generated electric energy of the TEG system under seven ECE cycles is obtained and compared. Here, the generated electric energy predicted by the steady-state numerical simulation is 1828.68 J, in which the average exhaust temperature and average exhaust mass flow rate of seven ECE cycles are used as the boundary conditions. The total generated electric energy of the TEG system under seven ECE cycles predicted by transient numerical simulation is 1624.07 J. The generated electric energy predicted by steady-state numerical simulation is 12.6% higher than that predicted by transient numerical simulation. Consequently, adopting the transient fluid-thermal-electric multiphysics coupling field numerical model is recommended to assess the performance of an automotive TEG system.

5. Conclusions

In this work, a transient fluid-thermal-electric multiphysics coupling field numerical model was proposed for the first time to study the dynamic performance of a simplified thermoelectric generator

system for automotive exhaust waste heat recovery. The transient exhaust characteristics of a conventional vehicle in seven ECE cycles were used as the inlet boundary conditions of the transient numerical model, including exhaust temperature and exhaust mass flow rate. Before the transient numerical simulations, the steady-state performance investigation on the thermoelectric generator system was conducted to obtain the maximum power point, and the corresponding load resistance was adopted in the transient performance analysis. In addition, the model validation was conducted via experimental tests at transient-state working conditions. The transient numerical simulations of the thermoelectric generator system were then performed, and the dynamic response characteristics of the output voltage, output power, and conversion efficiency were obtained and analyzed. Finally, the output power obtained from the steady-state numerical analysis was compared with that from the transient numerical analysis. According to the above numerical study, the following conclusions can be drawn:

(1) The proposed transient fluid-thermal-electric multiphysics coupling field numerical model can be used to predict the dynamic performance of automotive thermoelectric generator systems, with the consideration of dynamic characteristics, fluid-thermal-electric multiphysics field coupling effects, and material temperature dependence. Compared with the previous dynamic performance prediction methods, the proposed model has incomparable reasonableness and accuracy. The validity of the transient numerical model is experimentally verified via a designed transient performance test bench. The average error of transient output voltage between numerical results and experimental results is 9.24%.

(2) Detailed physical field distribution characteristics of the thermoelectric generator system can be obtained by solving the proposed model via COMSOL, including temperature distributions, voltage distributions, and current density distributions. Through a steady-state performance analysis, the maximum power point of $R_L = 4\ \Omega$ is obtained and selected for the transient numerical simulations.

(3) There is a delay in the output response of the thermoelectric generator system when the exhaust temperature remains a smooth change, and the change of output voltage and output power is often accompanied by the change of exhaust mass flow rate. The small and short-term fluctuation of exhaust gases has a slight influence on the output voltage and output power.

(4) With the transient change of exhaust characteristics, the output voltage and output power show more stable changes and slower responses, but the situation for conversion efficiency is the opposite. The conversion efficiency mainly depends on the exhaust mass flow rate, and its changing trend is opposite to that of the exhaust mass flow rate.

(5) Under seven ECE cycles, the generated electric energy of the thermoelectric generator system predicted by the steady-state numerical simulation is 1828.68 J, which is 12.6% higher than the 1624.07 J predicted by the transient numerical simulation. Steady-state performance analysis of automotive thermoelectric generator systems will lead to the overestimation of the output performance. Using the transient numerical model presented in this paper is suggested to conduct the dynamic performance analysis.

Acknowledgements

The authors are grateful for the financial support from the National Natural Science Foundation of China (51977100), EU ThermaSMART project under Grant No. H2020-MSCA-RISE (778104), as well as Ningbo Science and Technology Bureau's Technology under Grant No. 2019B10042. D. Luo acknowledges the financial support from China Scholarship Council (CSC).

References

[1] Dominković DF, Bačeković I, Pedersen AS, Krajačić G. The future of transportation in sustainable energy systems: Opportunities and barriers in a clean energy transition. Renewable Sustainable Energy Rev 2018;82:1823-38.

[2] Luo D, Wang R, Yu W, Sun Z, Meng X. Modelling and simulation study of a converging thermoelectric generator for engine waste heat recovery. Appl Therm Eng 2019;153:837-47.

[3] Li B, Huang K, Yan Y, Li Y, Twaha S, Zhu J. Heat transfer enhancement of a modularised thermoelectric power generator for passenger vehicles. Appl Energy 2017;205:868-79.

[4] Ge M, Li Z, Wang Y, Zhao Y, Zhu Y, Wang S, et al. Experimental study on thermoelectric power generation based on cryogenic liquid cold energy. Energy. 2021;220:119746.

[5] Tian H, Chang L, Gao Y, Shu G, Zhao M, Yan N. Thermo-economic analysis of zeotropic mixtures based on siloxanes for engine waste heat recovery using a dual-loop organic Rankine cycle (DORC). Energy Convers Manage 2017;136:11-26.

[6] Huang K, Yan Y, Wang G, Li B. Improving transient performance of thermoelectric generator by integrating phase change material. Energy. 2021;219:119648.

[7] Zhang Y, Cleary M, Wang X, Kempf N, Schoensee L, Yang J, et al. High-temperature and high-power-density nanostructured thermoelectric generator for automotive waste heat recovery. Energy Convers Manage 2015;105:946-50.

[8] Frobenius F, Gaiser G, Rusche U, Weller B. Thermoelectric Generators for the Integration into

Automotive Exhaust Systems for Passenger Cars and Commercial Vehicles. J Electron Mater 2016;45:1433-40.

[9] Yang H, Shu G, Tian H, Ma X, Chen T, Liu P. Optimization of thermoelectric generator (TEG) integrated with three-way catalytic converter (TWC) for harvesting engine's exhaust waste heat. Appl Therm Eng 2018;144:628-38.

[10] Wan Q, Liu X, Gu B, Bai W, Su C, Deng Y. Thermal and acoustic performance of an integrated automotive thermoelectric generation system. Appl Therm Eng 2019;158:113802.

[11] Fernández-Yañez P, Armas O, Capetillo A, Martínez-Martínez S. Thermal analysis of a thermoelectric generator for light-duty diesel engines. Appl Energy 2018;226:690-702.

[12] Wang Y, Li S, Xie X, Deng Y, Liu X, Su C. Performance evaluation of an automotive thermoelectric generator with inserted fins or dimpled-surface hot heat exchanger. Appl Energy 2018;218:391-401.

[13] Zhao Y, Wang S, Ge M, Liang Z, Liang Y, Li Y. Performance investigation of an intermediate fluid thermoelectric generator for automobile exhaust waste heat recovery. Appl Energy 2019;239:425-33.

[14] Huang G-Y, Hsu C-T, Fang C-J, Yao D-J. Optimization of a waste heat recovery system with thermoelectric generators by three-dimensional thermal resistance analysis. Energy Convers Manage 2016;126:581-94.

[15] Wang Y, Dai C, Wang S. Theoretical analysis of a thermoelectric generator using exhaust gas of vehicles as heat source. Appl Energy 2013;112:1171-80.

[16] Liu C, Deng YD, Wang XY, Liu X, Wang YP, Su CQ. Multi-objective optimization of heat exchanger in an automotive exhaust thermoelectric generator. Appl Therm Eng 2016;108:916-26.

[17] Massaguer A, Massaguer E, Comamala M, Pujol T, González JR, Cardenas MD, et al. A method to assess the fuel economy of automotive thermoelectric generators. Appl Energy 2018;222:42-58.

[18] Pacheco N, Brito FP, Vieira R, Martins J, Barbosa H, Goncalves LM. Compact automotive thermoelectric generator with embedded heat pipes for thermal control. Energy. 2020;197:117154.

[19] Luo D, Wang R, Yu W. Comparison and parametric study of two theoretical modeling approaches based on an air-to-water thermoelectric generator system. J Power Sources 2019;439:227069.

[20] He W, Guo R, Liu S, Zhu K, Wang S. Temperature gradient characteristics and effect on optimal

thermoelectric performance in exhaust power-generation systems. Appl Energy 2020;261:114366.

[21] Luo D, Wang R, Yu W, Zhou W. Parametric study of a thermoelectric module used for both power generation and cooling. Renewable Energy 2020;154:542-52.

[22] Chen W-H, Liao C-Y, Hung C-I. A numerical study on the performance of miniature thermoelectric cooler affected by Thomson effect. Appl Energy 2012;89:464-73.

[23] Luo D, Wang R, Yu W, Zhou W. A novel optimization method for thermoelectric module used in waste heat recovery. Energy Convers Manage 2020;209:112645.

[24] Luo D, Wang R, Yu W, Zhou W. A numerical study on the performance of a converging thermoelectric generator system used for waste heat recovery. Appl Energy 2020;270:115181.

[25] Crane D, LaGrandeur J, Jovovic V, Ranalli M, Adldinger M, Poliquin E, et al. TEG On-Vehicle Performance and Model Validation and What It Means for Further TEG Development. J Electron Mater 2013;42:1582-91.

[26] Massaguer A, Massaguer E, Comamala M, Pujol T, Montoro L, Cardenas MD, et al. Transient behavior under a normalized driving cycle of an automotive thermoelectric generator. Appl Energy 2017;206:1282-96.

[27] Lan S, Yang Z, Chen R, Stobart R. A dynamic model for thermoelectric generator applied to vehicle waste heat recovery. Appl Energy 2018;210:327-38.

[28] Meng J-H, Zhang X-X, Wang X-D. Characteristics analysis and parametric study of a thermoelectric generator by considering variable material properties and heat losses. Int J Heat Mass Transfer 2015;80:227-35.

[29] Fraisse G, Ramousse J, Sgorlon D, Goupil C. Comparison of different modeling approaches for thermoelectric elements. Energy Convers Manage 2013;65:351-6.

[30] Gou X, Yang S, Xiao H, Ou Q. A dynamic model for thermoelectric generator applied in waste heat recovery. Energy. 2013;52:201-9.

[31] Chen W-H, Lin Y-X, Wang X-D, Lin Y-L. A comprehensive analysis of the performance of thermoelectric generators with constant and variable properties. Appl Energy 2019;241:11-24.

[32] Yan Y, Malen JA. Periodic heating amplifies the efficiency of thermoelectric energy conversion. Energy Environ Sci 2013;6:1267-73.

[33] Meng J-H, Zhang X-X, Wang X-D. Dynamic response characteristics of thermoelectric generator predicted by a three-dimensional heat-electricity coupled model. J Power Sources 2014;245:262-9.

[34] Mitrani D, Salazar J, Turó A, García MJ, Chávez JA. One-dimensional modeling of TE devices considering temperature-dependent parameters using SPICE. Microelectron J 2009;40:1398-405.

[35] Mitrani D, Salazar J, Turó A, García MJ, Chávez JA. Transient distributed parameter electrical analogous model of TE devices. Microelectron J 2009;40:1406-10.

[36] Liang X, Sun X, Tian H, Shu G, Wang Y, Wang X. Comparison and parameter optimization of a two-stage thermoelectric generator using high temperature exhaust of internal combustion engine. Appl Energy 2014;130:190-9.

[37] Hu X, Jood P, Ohta M, Kunii M, Nagase K, Nishiate H, et al. Power generation from nanostructured PbTe-based thermoelectrics: comprehensive development from materials to modules. Energy Environ Sci 2016;9:517-29.

[38] Luo D, Yan Y, Wang R, Zhou W. Numerical investigation on the dynamic response characteristics of a thermoelectric generator module under transient temperature excitations. Renewable Energy 2021;170:811-23.

[39] Fisac M, Villasevil FX, López AM. Design of a thermoelectric generator with fast transient response. Renewable Energy 2015;81:658-63.

[40] Meng F, Chen L, Feng Y, Xiong B. Thermoelectric generator for industrial gas phase waste heat recovery. Energy. 2017;135:83-90.

[41] Bai W, Yuan X, Liu X. Numerical investigation on the performances of automotive thermoelectric generator employing metal foam. Appl Therm Eng 2017;124:178-84.

[42] Li W, Peng J, Xiao W, Wang H, Zeng J, Xie J, et al. The temperature distribution and electrical performance of fluid heat exchanger-based thermoelectric generator. Appl Therm Eng 2017;118:742-7.

[43] Ma T, Lu X, Pandit J, Ekkad SV, Huxtable ST, Deshpande S, et al. Numerical study on thermoelectric–hydraulic performance of a thermoelectric power generator with a plate-fin heat exchanger with longitudinal vortex generators. Appl Energy 2017;185:1343-54.

[44] Young DF, Munson BR, Okiishi TH, Huebsch WW. A brief introduction to fluid mechanics: John Wiley & Sons; 2010.

[45] Cao Q, Luan W, Wang T. Performance enhancement of heat pipes assisted thermoelectric generator for automobile exhaust heat recovery. Appl Therm Eng 2018;130:1472-9.